



HAL
open science

Contribution on the Source Field Calculation through the Biot-Savart Equation Using Curvilinear Elements and an Adaptive Process

Anderson Santos Nunes, Olivier Chadebec, Patrick Kuo-Peng, Patrick Dular, Bruno Cucco

► **To cite this version:**

Anderson Santos Nunes, Olivier Chadebec, Patrick Kuo-Peng, Patrick Dular, Bruno Cucco. Contribution on the Source Field Calculation through the Biot-Savart Equation Using Curvilinear Elements and an Adaptive Process. Progress In Electromagnetics Research C, 2018, 88, pp.145-161. 10.2528/PIERC18081004 . hal-01985762

HAL Id: hal-01985762

<https://hal.science/hal-01985762>

Submitted on 14 Nov 2019

HAL is a multi-disciplinary open access archive for the deposit and dissemination of scientific research documents, whether they are published or not. The documents may come from teaching and research institutions in France or abroad, or from public or private research centers.

L'archive ouverte pluridisciplinaire **HAL**, est destinée au dépôt et à la diffusion de documents scientifiques de niveau recherche, publiés ou non, émanant des établissements d'enseignement et de recherche français ou étrangers, des laboratoires publics ou privés.

Contribution on the Source Field Calculation through the Biot-Savart Equation Using Curvilinear Elements and an Adaptive Process

Anderson Nunes^{1, 2, *}, Olivier Chadebec³, Patrick Kuo-Peng¹,
Patrick Dular⁴, and Bruno Cucco⁵

Abstract—The analytical solution of the Biot-Savart equation can be complex in some cases, and its numerical integration is commonly more appropriate. In this paper, it is integrated using the Gauss-Legendre method through 1, 2 and 3-D domains, using first and second-order (curvilinear) isoparametric mapping. In order to verify the gain of accuracy with second-order elements, the results obtained are compared with analytical cases and with the Finite Element Method. Then this paper presents an adaptive method which profits from the accuracy along those elements with higher energy values, by reducing the number of Gauss points along the elements with lower energy. This approach reduces the total number of Gauss points evaluated during the integration process and provides a possibility to choose an interesting trade-off between simulation time and accuracy.

1. INTRODUCTION

The calculation of magnetic fields is one important part of the magnetic device modeling using both analytical and numerical approaches, the Biot-Savart equation [13] being largely applied in these two cases.

Extensive literature is available about calculating magnetic fields with the Biot-Savart equation, from more theoretical discussions as presented in [17] to specific applications [15, 24–28, 31]. Some developments based on a sort of geometric discretization are published in [1, 4, 10, 16, 21, 29, 30].

Regarding the numerical methods, there are many packages available to solve electromagnetic problems, in both high and low frequencies. Considering the packages applied to low frequency or even magnetostatic cases, it is possible to identify several applications of Biot-Savart, once some formulations require an “*a priori*” source field solution, for instance, in Finite Element Method (FEM) [20], in Facet Finite Element Method (FFEM) [22] as well as in some integral methods [9, 18, 19]. In [5] the BS field is used as an unperturbed solution in the subproblem technique. In the Computational Fluid Dynamics (CFD), the BS is applied to model the velocity field generated by distributed vorticity fields [3, 23, 32].

Even in numerical methods, the source field solution can be obtained using the analytical expressions given in the above references, respecting their specific topologies. However, for more complex geometries, end windings [16] for example, it can be difficult to obtain one analytical solution. So, the common sense is to performed the BS integration using the Gaussian quadrature [11] which is a more general approach, but whose accuracy depends on the discretization level and on the elements order.

Received 10 August 2018, Accepted 5 November 2018, Scheduled 18 November 2018

* Corresponding author: Anderson Nunes (nunes.anderson@gmail.com).

¹ GRUCAD/UFSC — Universida de Federal de Santa Catarina, Florianópolis, CEP: 88040-970, Brazil. ² GeePs — Group of Electrical Engineering — Paris, CNRS, Centrale Supélec, Université Paris-Sud, Université Paris-Saclay, Sorbonne Université, 3 & 11 rue Joliot-Curie, Plateau de Moulon 91192 Gif-sur-Yvette CEDEX, France. ³ Université Grenoble Alpes, CNRS, G2Elab, F-38000 Grenoble, France. ⁴ University of Liège, Department of Electrical Engineering and Computer Science, ACE, Liège B-4000, Belgium.

⁵ Institute of Exact Sciences/UFMG — Universida de Federal de Minas Gerais, Belo Horizonte, CEP: 31270-901, Brazil.

Hence, in order to study the effectiveness of higher order elements, in this paper, the Biot-Savart equation is integrated through the Gaussian quadrature method using first and second-order elements with isoparametric mapping in 1-D (in a 3-D Lagrangian space), 2-D and 3-D. For each case, i.e., 1, 2 and 3-D domains, one coarse and one refined meshes are generated. Then, each of these meshes is used to solve the problems through first and second-order elements. The results are compared with exact analytical solutions or with the FEM, allowing to analyze the accuracy obtained with first and second-order elements.

Furthermore, obtaining the magnetic field using Biot-Savart along large domains can be a time-consuming task. With the aim of mitigating this issue, one simple adaptive algorithm is presented that selects those elements with high energy levels considering the magnetic field obtained at only one Gauss point. Along these elements, the integration is reevaluated taking into account all the Gauss points. However, along those low energy elements, the magnetic field is assumed to be constant, and consequently, only one Gauss point can be considered, reducing the total number of Gauss points evaluated during the integration process. The CPU time is compared with the classical solution, which considers all the Gauss points of all elements. Then, in order to make sure that this is a coherent approach in terms of physical precision, the magnetic field obtained using this algorithm is used in the FFEM [22] as a source field, and the results, i.e., magnetic induction and energy, are solved in a 3-D device and compared.

2. THE BIOT-SAVART EQUATION

Given a non-magnetic domain Ω with the conductive and stranded region Ω_s fed by the current density \mathbf{J} , Fig. 1, the magnetic field at the point $Q \in \Omega$ can be obtained using

$$\mathbf{H}(Q) = \frac{1}{4\pi} \int_{\Omega_{sv}} \frac{\mathbf{J}(P) \times \mathbf{r}_{PQ}}{|\mathbf{r}_{PQ}|^3} d\Omega_{sv} \quad (1)$$

where $P \in \Omega_s$ is the Gauss integration point, and \mathbf{r}_{PQ} is the position vector between Q and P .

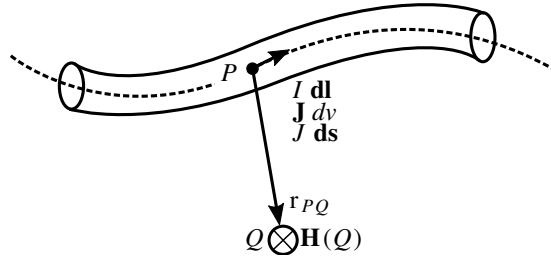


Figure 1. Integration domain for the Biot-Savart equation.

In some cases, Ω_s can be simplified by its average line, consequently not requiring a 3-D but 1-D mesh [27] which could represent some computational advantages. In this case, the magnetic field is calculated by:

$$\mathbf{H}(Q) = \frac{I}{4\pi} \int_{\Omega_{sl}} \frac{d\mathbf{l}(P) \times \mathbf{r}_{PQ}}{|\mathbf{r}_{PQ}|^3} d\Omega_{sl} \quad (2)$$

For 2-D symmetries, Eq. (1) can be rewritten as

$$\mathbf{H}(Q) = \frac{J}{2\pi} \int_{\Omega_{ss}} \frac{d\mathbf{s}(P) \times \mathbf{r}_{PQ}}{|\mathbf{r}_{PQ}|^2} d\Omega_{ss} \quad (3)$$

If the mesh in Ω is composed by first-order elements, the integration process along Ω_s can be done based on a non-conform mesh in Ω , allowing the use of higher order isoparametric elements, for instance, increasing the accuracy mainly when Ω_s is composed by curved bodies. Perhaps it is important to notice that this gain of accuracy does not solve the well-known singularity problem that happens when the

$|\mathbf{r}_{PQ}|$ tends to zero. In the case of time-varying formulations, it is possible to speed up the CPU time by normalizing the current in the conductors as 1 A, for instance, and multiplying the field by the real currents afterward. Also, as the conductors are immersed in a region with $\mu_r = 1$, it is possible to explore symmetries, which can be lost in the complete problem [7].

Regarding the CFD cases, the Biot-Savart equation is used to obtain the velocity field, \mathbf{V} , due to the vorticity \mathbf{W} , i.e.,

$$\mathbf{V}_{(Q)} = -\frac{1}{4\pi} \int_0^\pi \int_0^\pi \int_{-\infty}^\infty \mathbf{S} \times \mathbf{W}_{(P)} \sin \phi \, d\phi \, d\theta \, dr \quad (4)$$

once $\text{curl } \mathbf{V} = \mathbf{W}$. $\mathbf{r}_{PQ} = -R\mathbf{S}$ and $\mathbf{S} = (\sin \phi \cos \phi, \sin \phi \sin \theta, \cos \phi)$ is the radius unit vector. In this case, it is common to apply the equation in spherical coordinates, eliminating the singularity in the integrand and making the integration easier in the numerical standpoint [3].

Besides that, it is possible to apply the Biot-Savart equation using other coordinate systems, spherical or cylindrical one [10] for example, Eqs. (1), (2) and (3) are implemented using the cartesian system.

The integration process is performed using the well-known Gauss quadrature [2], and the mapping of the points P and Q is obtained with the shape functions corresponding to each element type. The element order and the number of integration points are specified for each analyzed domain type. As these topics are already well established, and for the sake of brevity, they are not presented here.

3. CURVED ELEMENTS MAPPING

It is known that curved elements can provide higher accuracy when modeling geometries with curved topologies [14]. This mapping can be accomplished by transforming one curved element in the Euclidean $\Omega(xyz)$ space into a reference element with straight sides and flat faces $\hat{\Omega}(u, v, w)$ space.

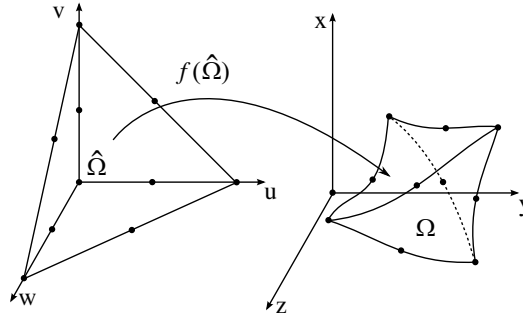


Figure 2. Coordinates mapping.

Given the reference element $\hat{\Omega}$, Fig. 2, it is possible to map any coordinate into the real element, Ω

$$\begin{aligned} x &= \sum_{i=1}^{n_e} N_i^e(u, v, w) x_i \\ y &= \sum_{i=1}^{n_e} N_i^e(u, v, w) y_i \\ z &= \sum_{i=1}^{n_e} N_i^e(u, v, w) z_i \end{aligned} \quad (5)$$

where N_i^e is the nodal shape functions; i is the element node index; and n_e is the number of element nodes. The N_i^e functions applied in this work are given in [12], and its specific table of each of the N_i^e functions is summarized in Table 1.

Table 1. Tables with the N_i^e functions in [12]

Element type	First-order	Second-order
1-D (line)	Table 8.2	Table 8.3
2-D (triangle)	Table 8.4	Table 8.5
3-D (tetrahedral)	Table 8.9	Table 8.10

Regarding the integration process, it could be done analytically along straight elements with linear shape functions. However, this is not the case for the curvilinear elements, where the non-polynomial variations may happen in the integrands. In these cases, the numerical integration methods are more indicated [20], and taking into account its application on the FEM, the Gaussian quadrature is applied, i.e.,

$$\int K(u) du = \sum_{i=1}^r W_i K(u_i) \quad (6)$$

where r is the number of Gauss points, and W is the weight associated to each point.

The number of Gauss points used for each type of element are indicated in Table 2 and can be found in details in [2, 12, 20].

Table 2. Number of Gauss points used in this work.

Element type	First-order	Second-order
1-D (line)	1	2
2-D (triangle)	3	4
3-D (tetrahedral)	4	5

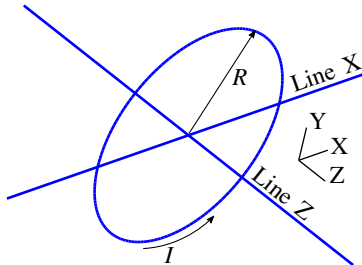
4. RESULTS

Considering the aim of this work, all the results presented are obtained considering the integration of Equations (1), (2) and (3), through first and second-order elements of a coarse and a fine meshes. Then the results are compared between them, with analytical equations or with the FEM.

All the meshes presented in this work were generated using the Gmsh [8] program.

4.1. 1-D: A Current Loop

In some large-scale models, it is possible to neglect the cross-section of the conductors considering filament approximations [27]. So, the first test case is one circular loop fed by a current of $I = 100$ A, Fig. 3, where $R = 150$ mm. The coarse meshes generated, both with 8 elements, are presented in Fig. 4. It is noticeable that the discretization improvement is obtained with the second-order elements.

**Figure 3.** 1-D current loop.

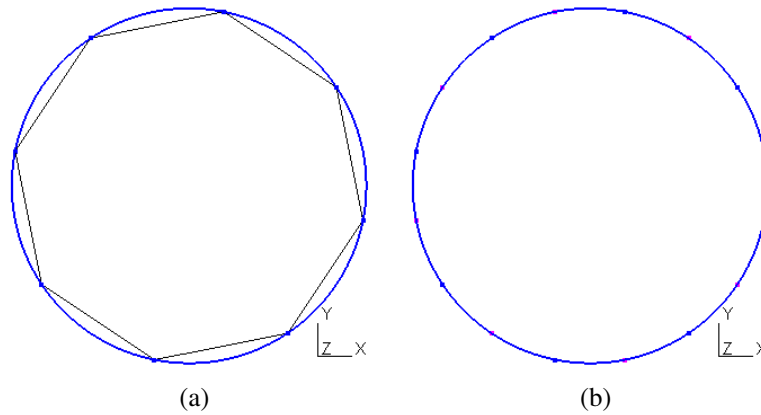


Figure 4. 1-D coarse mesh. (a) First-order. (b) Second-order.

The results obtained by integrating Eq. (2) along these meshes are compared with the analytical solution,

$$H_z = \frac{IR^2}{2(R^2 + z^2)^{3/2}} \tag{7}$$

along the line Z . For the particular case of $Z = 0$, i.e., in the center of the current loop, the magnetic field $H_z = 333.333$ A/m.

The results obtained using the coarse meshes are presented in Fig. 5, which shows a difference of proximately 15% in the results calculated with first-order elements and 0.1% in the results obtained with second-order elements.

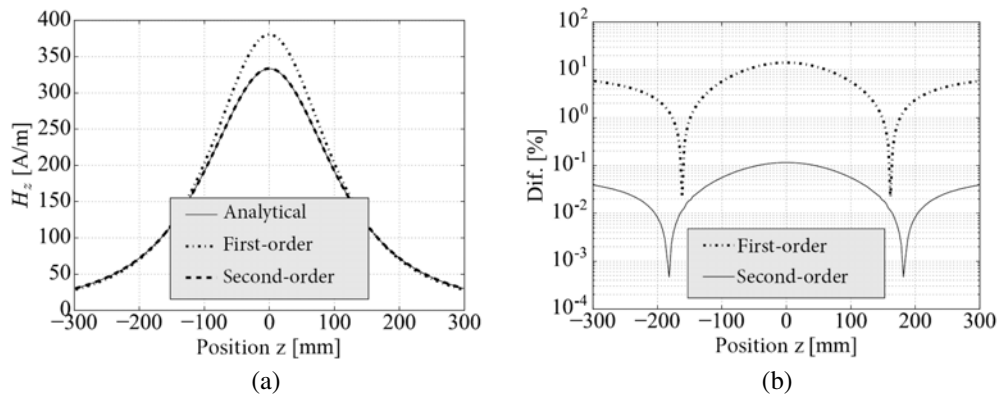


Figure 5. Line Z — Coarse mesh. (a) Magnetic field. (b) Comparison.

Then, this 1-D mesh is regenerated with 32 elements, and the new results are shown in Fig. 6. In this case, the differences are 0.8% and $5 \cdot 10^{-4}\%$.

For the analysis along the X axis (line X in Fig. 3), the results obtained with the coarse mesh are given in Fig. 7, where the blue lines represent the conductors positions.

As expected in a BS solution, the field intensity increases drastically when the distance between the analysis point and the conductor is small. This behavior is clear when the second-order elements are used, but the lack of precision of the first-order solution does not show this behavior properly. On the other hand, when this distance increases, the differences between the results decrease.

The results obtained with the refined mesh, Fig. 8, are more coherent, but the magnetic field closer to the conductor is considerably higher when calculated with second-order elements. However, the results are more similar for far regions, with a difference of 0.7% at the center of the loop, i.e., $x = 0$.

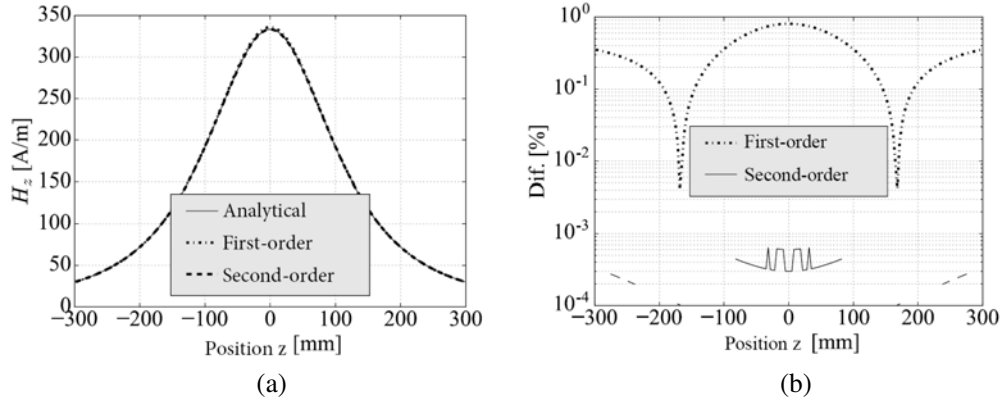


Figure 6. Line Z — Fine mesh. (a) Magnetic field. (b) Comparison.

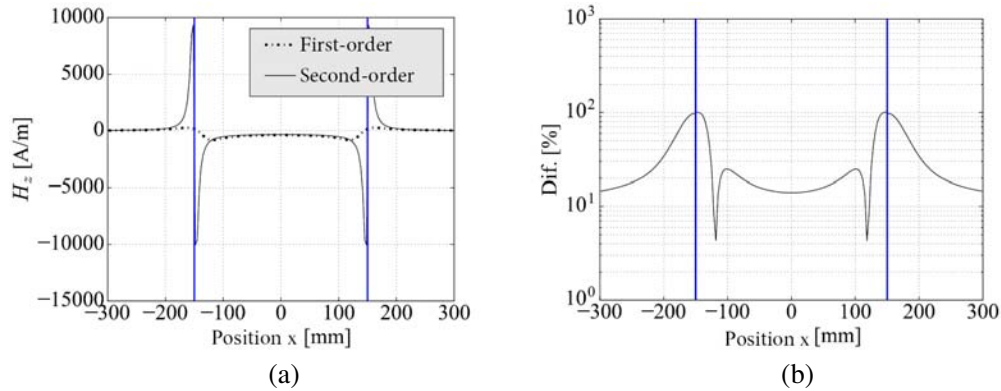


Figure 7. Line X — Coarse mesh. (a) Magnetic field. (b) Comparison.

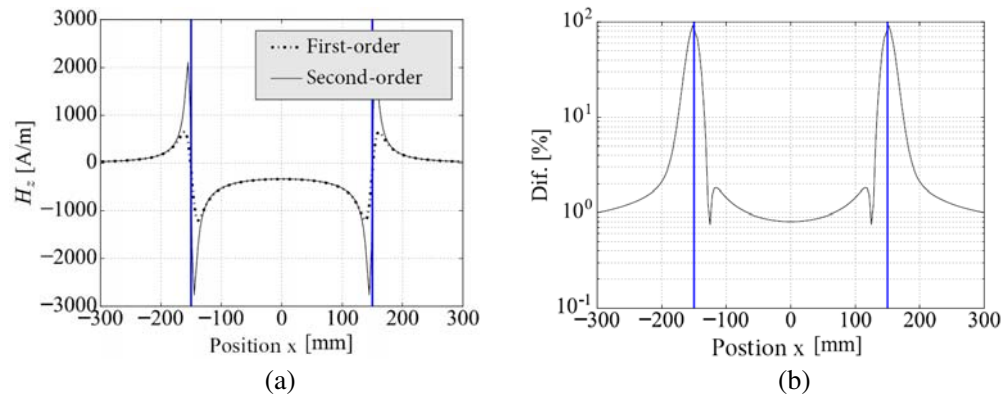


Figure 8. Line X — Fine mesh. (a) Magnetic field. (b) Comparison.

Regarding the computational time, as presented in Table 2, the first-order integration was implemented with one Gauss point and the second-order with two. So, one can expect the simulation time with second-order twice longer. For the coarse and refined meshes, this factor was 2.33 and 2.09, respectively. Hence comparing the results presented in Figs. 6(b) and 5(b), one realizes that the difference obtained with the second-order coarse mesh is about ten times lower than the difference verified with the first-order refined mesh. This fact suggests that a coarse mesh with second-order elements would be more appropriate.

4.2. 2-D: A Symmetry along the XY Plane

Regardless of the numerical method or formulation used, the 2-D symmetries are largely applied and worth this analysis. For this sake, a simple geometry is composed by two circular conductors and placed in the XY plane, as presented in Fig. 9, where $R_i = 25$ mm, $R_e = 50$ mm, $ly = 10$ mm and $J = 13333.33333$ A/m² in Z direction.

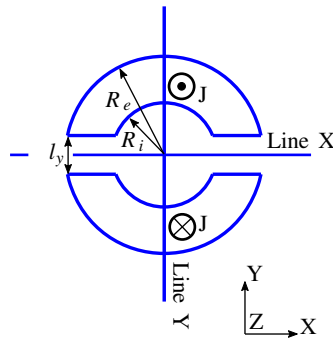


Figure 9. 2-D geometry.

The reference solution is obtained with the FEM method, with a magnetic vector potential \mathbf{A} formulation and an adequately refined second-order mesh, through the programs Gmsh [8] and GetDP [6]. The flux lines and the magnetic field distribution are shown in Fig. 10.

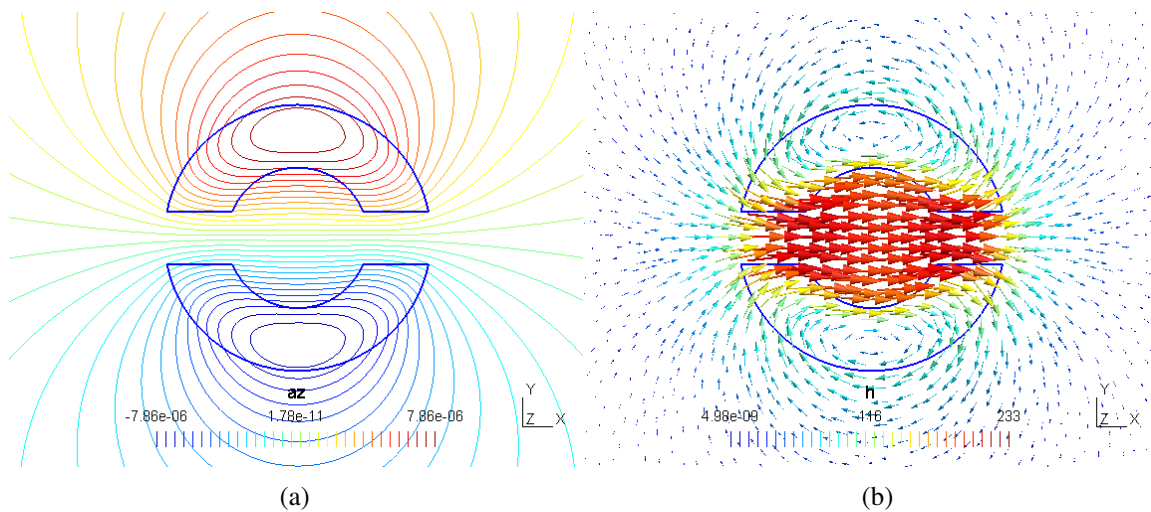


Figure 10. FEM solution. (a) Flux lines. (b) Magnetic field.

Then, the magnetic field distribution is calculated using the Biot-Savart equation given in Eq. (3) along the axes X and Y , lines X and Y of Fig. 9. The Gauss integration is performed using one and three points for the first and second-order elements, respectively. The two meshes, coarse and fine, count with 34 and 1210 elements, and the first of them is shown in Fig. 11.

The results obtained along the line X with the coarse mesh and the comparison with FEM are given in Fig. 12. The results present a maximum difference of 10% and 2.5% for elements of first and second-order. Notwithstanding, these differences are less significant at the center of the model ($x = 0$), i.e., 2% and 0.6%.

The fields calculated with the refined mesh, Fig. 13, are close and present a maximum difference of about 1.2%. At the center of the geometry, the difference is about 0.3%.

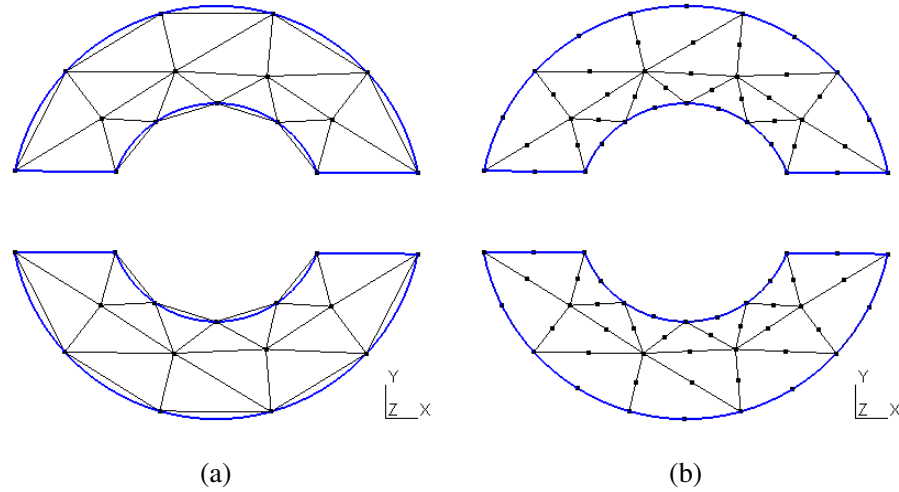


Figure 11. 2-D coarse mesh. (a) First-order. (b) Second-order.

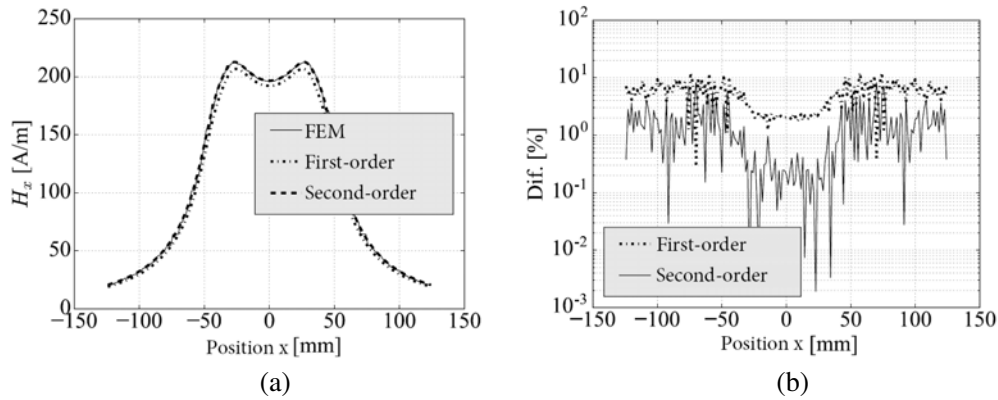


Figure 12. Line X — Coarse mesh. (a) Magnetic field. (b) Comparison.

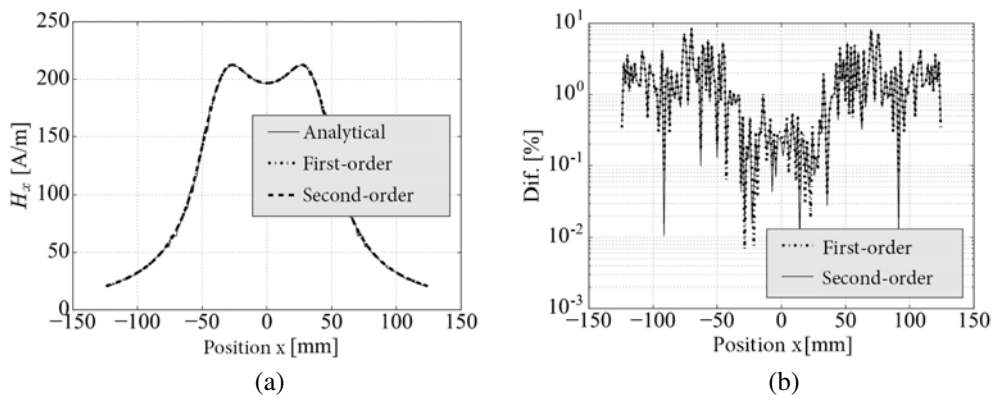


Figure 13. Line X — Fine mesh. (a) Magnetic field. (b) Comparison.

For the line Y, the results calculated with the coarse mesh are presented in Fig. 14. In this case, there are points of interest inside the conductive domain, delimited by each pair of blue lines in Fig. 14(a), which makes the application of the Biot-Savart equation more complex due to its singularity. This problem happens in both first and second-order cases and can generate important differences.

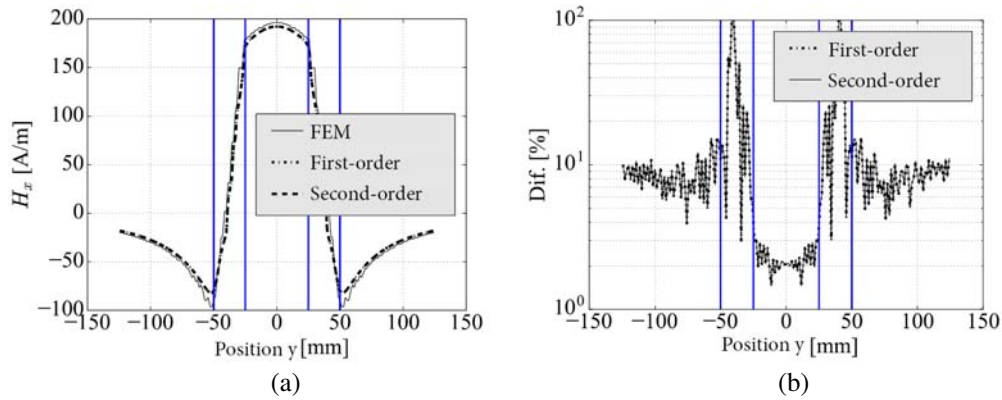


Figure 14. Line Y — Coarse mesh. (a) Magnetic field. (b) Comparison.

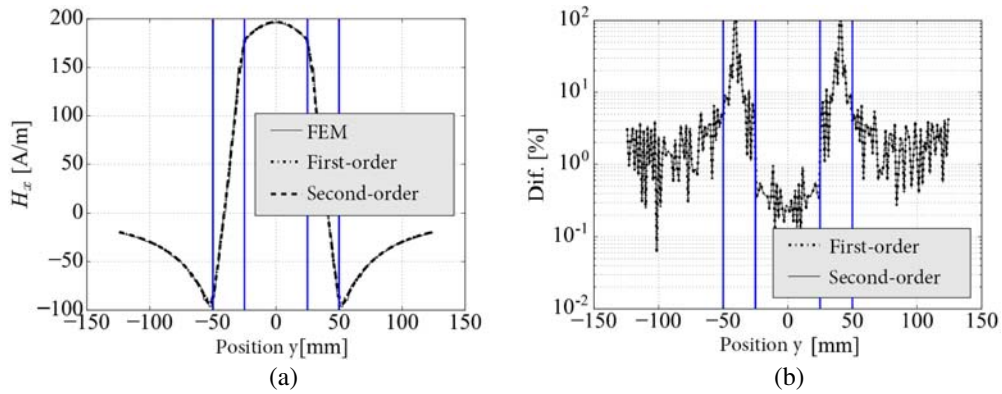


Figure 15. Line Y — Fine mesh. (a) Magnetic field. (b) Comparison.

One relevant aspect in Fig. 14(b) is that, beyond the singularity, the higher differences are due to the low value of the reference field, which crosses the zero in one point inside the conductive domain. These differences decrease significantly outside the conductive regions, Fig. 14(b) and Fig. 15(b).

As shown in Table 2, the expected computational time ratio between first and second-order would be about 1.33, once three and four Gauss points were used for the first and second-order elements, respectively. The real factor obtained was 1.67 and 1.98. The difference, if considering the ideal factor of 1.33, is due to the additional calculation need in the second-order coordinates mapping. Thus, comparing the results presented in Figs. 12(b) and 13(b) (or Figs. 14(b) and 15(b)), one can verify that the second-order coarse mesh has already presented an acceptable precision, if compared with the refined meshes (Figs. 13(b) and 15(b)), leading to conclusion that, as in the 1-D case, this would be a proper approach.

4.3. 3-D: A Cylindrical Conductor

For those problems where it is not possible to neglect the cross-section of the conductors neither to use 2-D symmetries, it is necessary to discretize the 3-D conductive domain and to define the current density field along it.

The test case is the long cylindrical conductor presented in Fig. 16, where $R_i = 45$ mm, $R_o = 60$ mm, $l_z = 500$ mm and $J = 13333.33333$ A/m².

The magnetic field is obtained along the lines X and Z, through the integral in Eq. (1) with first and second-order meshes, using four and five Gauss points in the integral evaluation, respectively. The

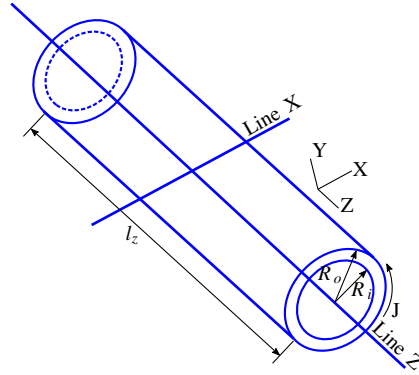


Figure 16. Cylindrical conductor geometry.

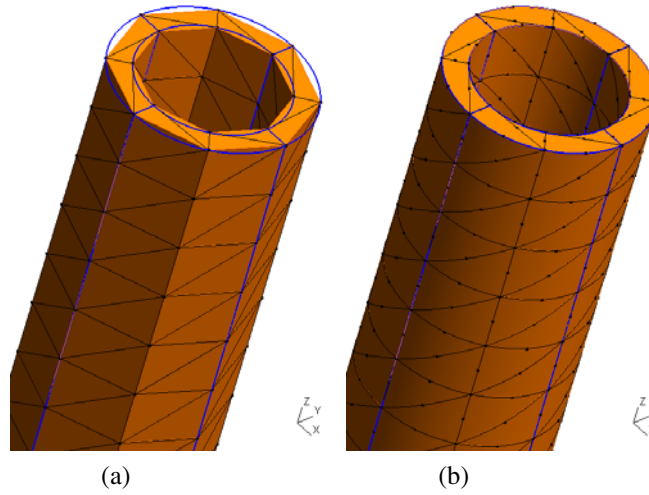


Figure 17. 3-D coarse mesh. (a) First-order. (b) Second-order.

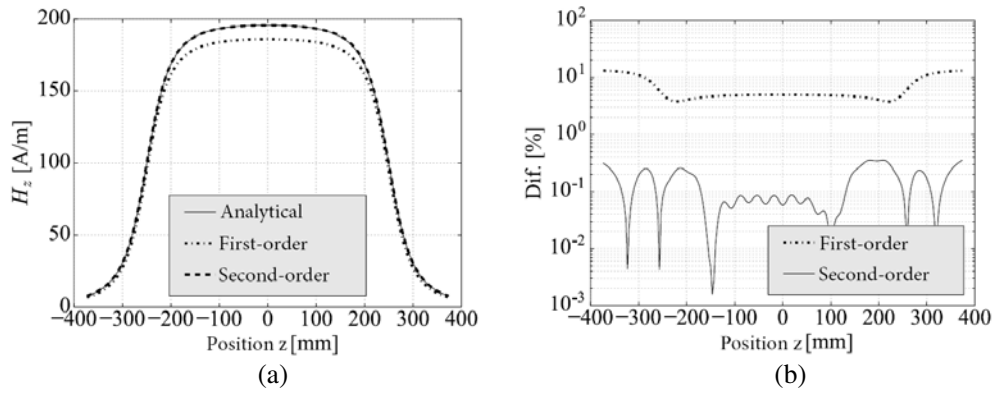


Figure 18. Line Z — Coarse mesh. (a) Magnetic field. (b) Comparison.

comparison is performed based on one analytical equation,

$$H_z = \frac{NI}{2l_z} \left[\left(\frac{\frac{l_z}{2} - z}{\sqrt{\left(z - \frac{l_z}{2}\right)^2 + R^2}} + \frac{\frac{l_z}{2} + z}{\sqrt{\left(z + \frac{l_z}{2}\right)^2 + R^2}} \right) \right] \quad (8)$$

Evaluating Eq. (8) at the center of the conductor, $x = 0, y = 0, z = 0$, with $N = 1$ and $I = 100$, the result is $H_z = 196.11$ A/m.

In the same way as that in the previous cases, a coarse (688 elements), Fig. 17, and a refined (6844 elements) meshes are used.

The results obtained along the Line Z and its comparison with Eq. (8) are given in Fig. 18 for the coarse mesh. The maximum differences obtained with first and second-order elements are 14% and 0.4%, respectively.

The magnetic fields obtained with the refined mesh are shown in Fig. 19, with differences of 1% and 0.3%, for first and second-order elements.

For the line X , the results calculated with the coarse mesh are presented in Fig. 20 and in Fig. 21

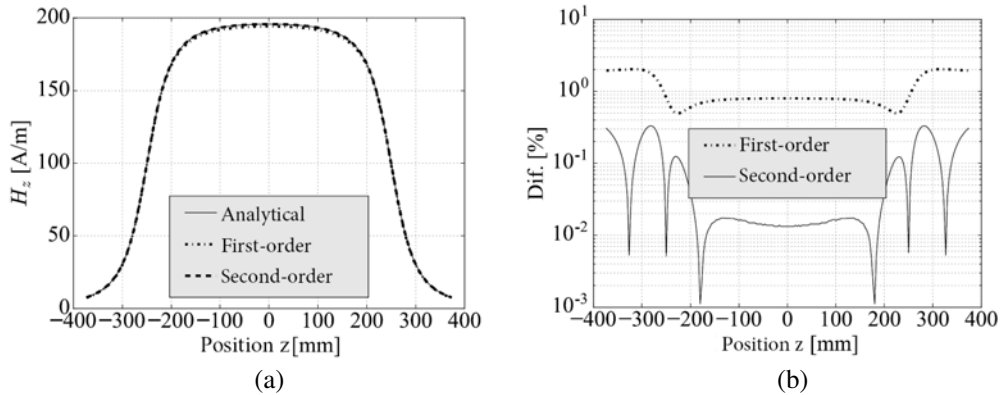


Figure 19. Line Z — Fine mesh. (a) Magnetic field. (b) Comparison.

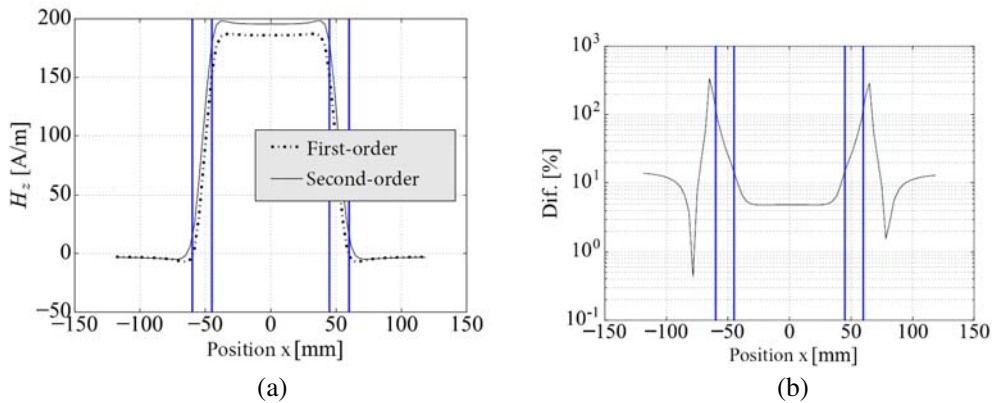


Figure 20. Line X — Coarse mesh. (a) Magnetic field. (b) Comparison.

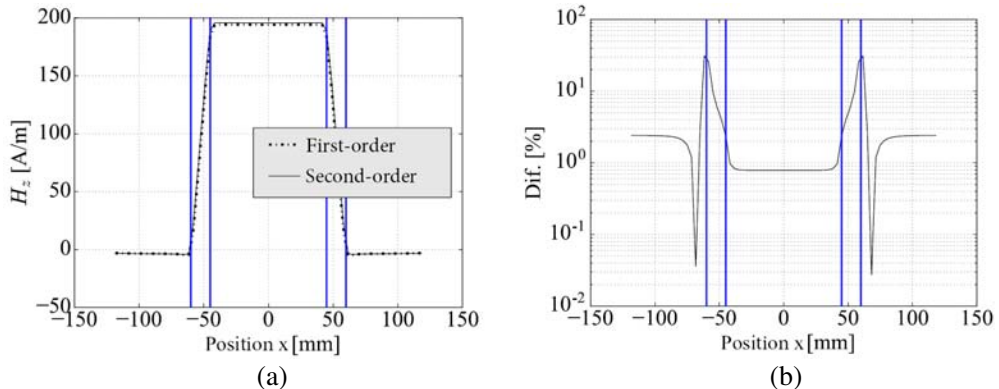


Figure 21. Line X — Fine mesh. (a) Magnetic field. (b) Comparison.

with the refined one. The blue lines in these figures present the limits of the conductive domains.

The results are very similar, but as the previous cases, it was found that the differences are more important inside the conductive domains. Outside, the absence of the singularity allows to obtain coherent results. For instance, it is possible to compare the field at the center of the conductor, where $H_z = 196.11$ A/m, in Eq. (8). At this point, the differences are 5% and 0.19%.

Comparing the computational time ratio between the solutions obtained with first and second-order elements, one could expect 1.25 times (see Table 2). In this case, it was 1.48 and 2.58. As already mentioned in the 2-D case, it is expected to have higher ratios if compared with the ideal, i.e., 1.25, once some additional calculations are needed when running the second-order elements. Considering this lower ratio for coarse meshes and comparing the results presented in the above figures, one can conclude that, mainly in 3-D, a coarse second-order mesh would be preferred instead of a refined first-order one.

4.4. Gauss Points

As the integrals in Eqs. (1), (2) and (3) are solved using the Gauss-Legendre integration method, the impact on the accuracy when using different numbers of integration points is analyzed. Considering that this method can integrate a polynomial order of $m \geq 2r - 1$ exactly [12], it would not be possible to obtain an appropriate accuracy with one integration point at this case. On the other hand, four points would be enough to solve the problem accurately.

For this sake, Eq. (1) is evaluated considering one, four and five Gauss points for the integration along the conductive domain given in Fig. 16 and considering the second-order coarse mesh. The Gauss points coordinates used here are presented in Table 8.11 of [12].

The magnetic field results along the Z line are presented in Fig. 22(a), while the comparison with the analytical solution is shown in Fig. 22(b). There is a considerable precision difference from one to four points which does not happen between four and five points.

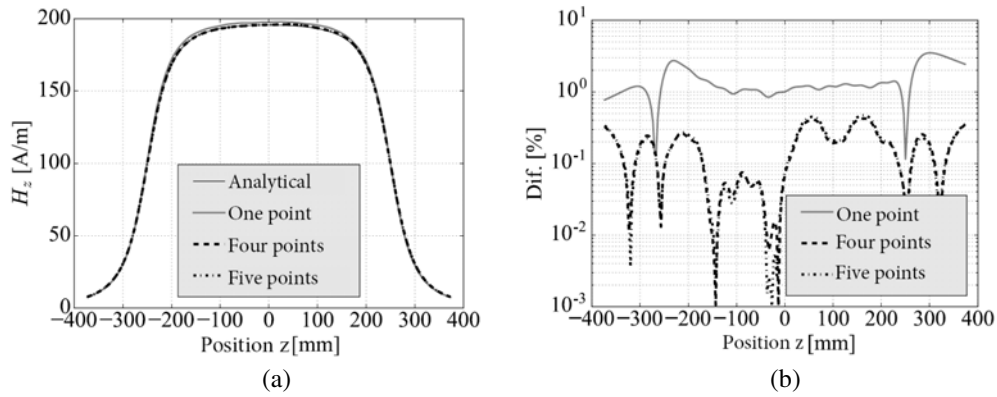


Figure 22. Line Z — Coarse mesh. (a) Magnetic field. (b) Comparison.

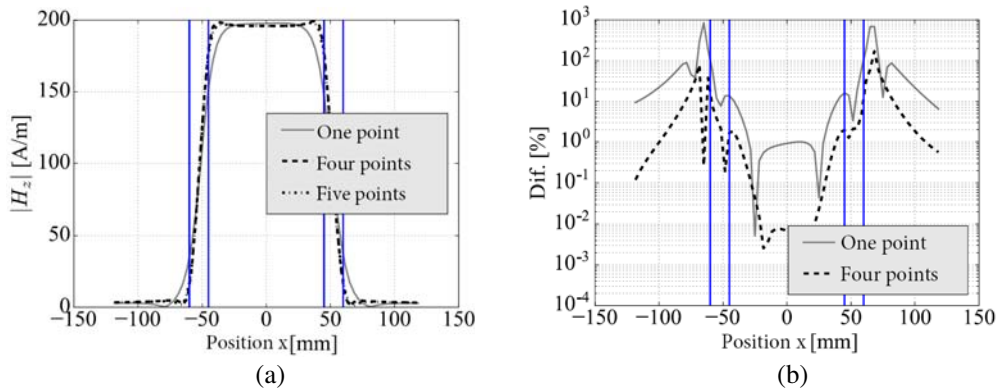


Figure 23. Line X — Coarse mesh. (a) Magnetic field. (b) Comparison.

As there is no analytical solution for the field along the line X , the results are compared between themselves in Fig. 23(a). The relative difference in relation to the results obtained with five points is presented in Fig. 23(b).

The differences are important between one and four points, which does not happen between four and five points. The results emphasize the importance of properly choosing the number of integration points based on the order of the function, as mentioned before and presented in Table 2.

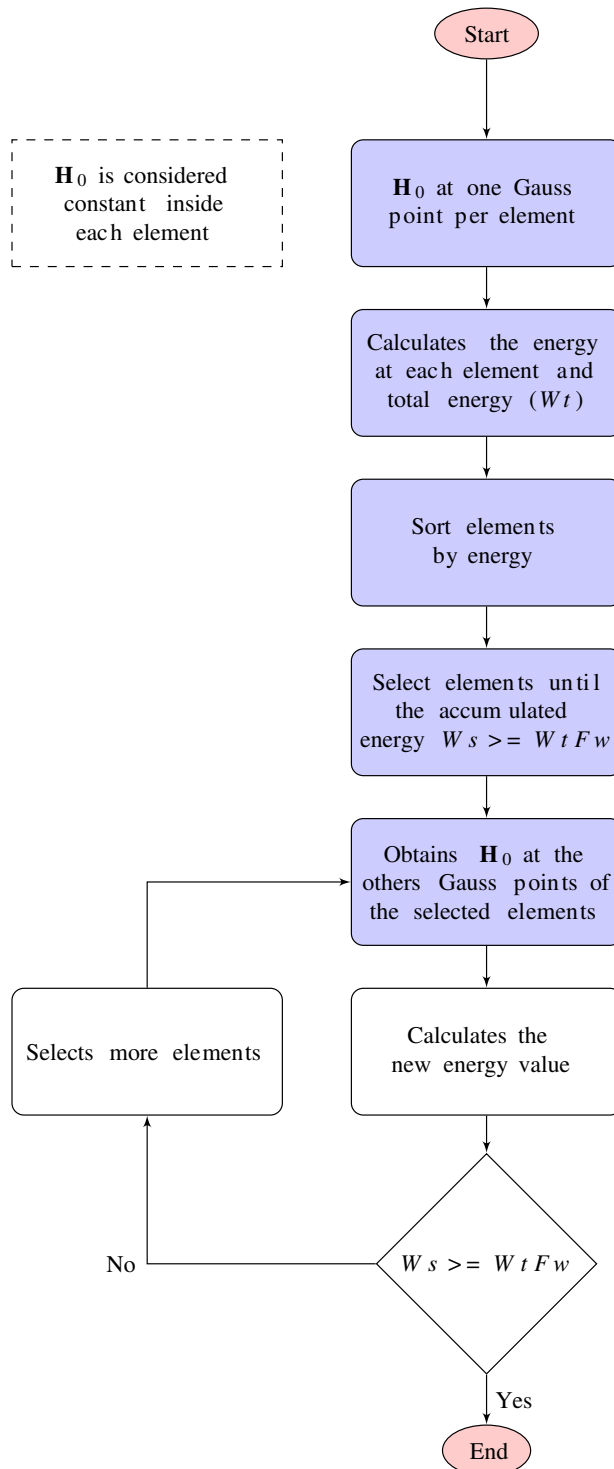


Figure 24. Flow chart of the adaptive process.

5. ADAPTIVE PROCESS

Even the isoparametric elements allow a gain of accuracy, the source field calculation with the Biot-Savart equation can be a time-consuming task, since it is necessary to integrate this equation for the Gauss points of all the elements in Ω . So, the following algorithm is proposed to mitigate its impact on the simulation time.

It is based on the assumption that the source magnetic field is constant inside each element of Ω with low magnetic energy level, and consequently, the negative impact of such an assumption is minimized because the method preserves the classical integration method (i.e., with all the Gauss points) along those regions of the domain with high energy levels.

Thus, based on this hypothesis, the magnetic field is calculated only at one Gauss point for all the elements of the domain. Then the magnetic energy of each element is calculated considering a constant magnetic field (one integration point), and the total energy along Ω , W_t , is obtained. Then, the elements are ordered based on their energy values, and those with higher energy are selected until the total energy of these elements, W_s in Fig. 24, is higher than a fraction Fw of the energy calculated in the first step. Finally, the magnetic field is calculated for the other Gauss points of those selected elements, as presented in the main chain of the flowchart given in Fig. 24.

Consequently, there is no loss of accuracy at those elements that store more energy, and the number of evaluations of the Biot-Savart equation can be drastically reduced.

Furthermore, after the selection of the elements, it is possible to recalculate the energy W_s and check if $W_s \geq W_t Fw$. If it is not true, it is possible to select more elements with high energy level.

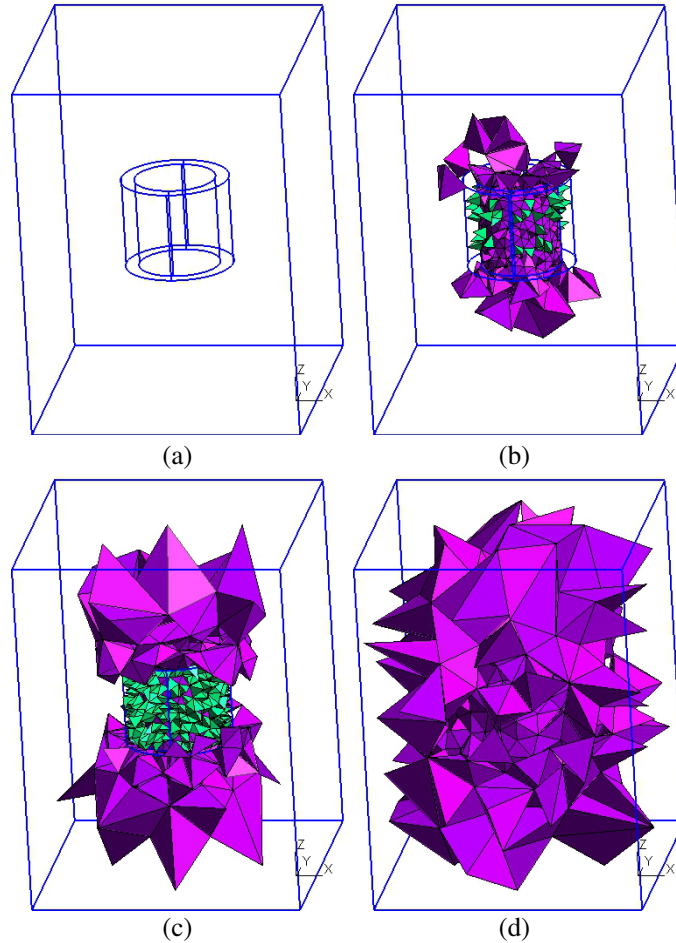


Figure 25. Geometry and selected elements. (c) $Fw = 0.8$. (d) $Fw = 0.95$.

This loop can be used to ensure a convergence based on the total energy along the domain.

The test case of this methodology consists of one winding with $R_i = 45$ mm, $R_o = 60$ mm, $l_z = 100$ mm and $J = 13333.33333$ A/m² placed inside one air region, as presented in Fig. 25(a). One mesh is generated, and the algorithm is run. The selected elements are depicted in Figs. 25(b), 25(c) and 25(d) for $Fw = 0.5$, $Fw = 0.8$ and $Fw = 0.95$, respectively. This means that along those elements, the magnetic field is calculated at all the Gauss points, but at only one point in the elements not shown.

The computational time comparison based on the conventional method that takes into account all the Gauss points of all the elements ($Fw = 1$ in this case) is presented in Table 3.

Table 3. Comparison with $Fw = 1.0$.

Fw	Simulation time [pu]	Magnetic energy [J]
0.5	0.52	59.14
0.8	0.70	57.23
0.95	0.86	56.86
1.0	1.0	58.4

Then, the magnetic field obtained for these cases are used as source fields in a magnetostatic Facet Finite Element Method formulation [22], and the magnetic flux density is obtained for a line placed in the center of the winding. The results are shown in Fig. 26.

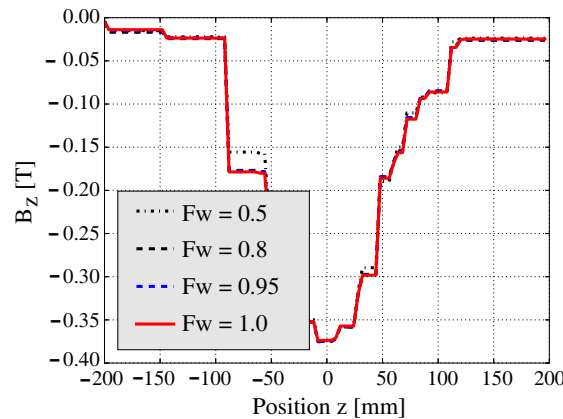


Figure 26. B_z along center line of the winding.

These results mean that the user can choose an Fw factor which best fits the accuracy needed, but based on the tests implemented in this work, about 0.8 would be an interesting trade-off between computational time and accuracy.

6. CONCLUSION

The Biot-Savart equation is largely applied to solve problems related to electromagnetics and fluid dynamics. Considering the numerical methods applied to model magnetic fields, this equation is important due to the formulations which require a source field solution.

However, this analysis has shown what its use implies in a previous investigation of the application and discretization, in order to avoid possible singular solutions, which can generate high local errors. On the other hand, the results are precise when the solution point is not so close to the integration points.

Analyzing the comparisons between the results obtained with first and second-order elements in the coarse meshes, one can verify how the results obtained with second-order elements are more accurate.

The computational time comparison between the first and second-order solutions shows that the ratio is not the same depending on the number of elements (coarse and fine meshes), but analyzing the gain of accuracy obtained with second-order elements, one can conclude that meshes with fewer second-order elements may represent a better option over more refined meshes with first-order elements.

Regarding the adaptive process presented, it was possible to reduce the simulation time, and it can represent an option to choose the best trade-off between simulation time and accuracy level. The solution used as a source field in the FFEM can suggest this methodology as a possible solution to mitigate the Biot-Savart impact on this kind of application.

REFERENCES

1. Azpurua, M. A., "A semi-analytical method for the design of coil-systems for homogeneous magnetostatic field generation," *Progress In Electromagnetics Research B*, Vol. 37, 171–189, 2012.
2. Bastos, J. P. A. and N. Sadowski, *Electromagnetic Modeling by Finite Element Methods*, Marcel Dekker, New York, 2003.
3. Carley, M., "Evaluation of Biot-Savart integrals on tetrahedral meshes," *SIAM Journal on Scientific Computing*, 2017.
4. Ciric, I. R., "Simple analytical expressions for the magnetic field of current coils," *IEEE Transactions on Magnetics*, Vol. 27, No. 1, 669–673, 1991.
5. Dular, P., "Modfielisation du champ magnfietique et des courants induits dans des systémes tridimensionnels non linéaires," Ph. d, Université de Liege, 1996.
6. Dular, P., C. Geuzaine, F. Henrotte, and W. Legros, "A general environment for the treatment of discrete problems and its application to the finite element method," *IEEE Transactions on Magnetics*, Vol. 34, No. 5, 3395–3398, September 1998.
7. Dular, P., L. Krähenbühl, M. V. Ferreira da Luz, P. Kuo-Peng, and C. Geuzaine, "Progressive inductor modeling via a finite element subproblem method," *COMPEL*, Vol. 34, No. 3, 851–863, May 2015.
8. Geuzaine, C. and J.-F. Remacle, "Gmsh: A 3-d finite element mesh generator with built-in pre- and post-processing facilities," *International Journal for Numerical Methods in Engineering*, Vol. 79, No. 11, 1309–1331, September 2009.
9. Guibert, A., J. L. Coulomb, O. Chadebec, and C. Rannou, "A post-processing integral formulation for the computation of magnetic field in conductors," *IEEE Transactions on Magnetics*, Vol. 47, No. 5, 1334–1337, 2011.
10. Gyimesi, M. G., D. Lavers, T. Pawlak, and D. Ostergaard, "Biot-savart integration for bars and Arcs," *IEEE Transactions on Magnetics*, Vol. 29, No. 6, 2389–2391, 1993.
11. Lee, H.-B. and H.-J. Song, "Efficient magnetic field calculation method for pancake coil using biot-savart law," *2006 12th Biennial IEEE Conference on Electromagnetic Field Computation*, Vol. 27, 193–193, IEEE, 2006.
12. Ida, N. and J. P. A. Bastos, *Electromagnetics and Calculation of Fields*, 2nd edition, Springer, New York, 1997.
13. Jackson, J. D., *Classical Electrodynamics*, 3rd edition, John Wiley & Sons, New York, 1999.
14. Jin, J.-M., *The Finite Element Method in Electromagnetics*, 2nd edition, A Wiley-Interscience Publication, Wiley, New York, 2002.
15. Kalhor, H. A., "Comparison of Ampere's circuital law (ACL) and the law of Biot-Savart (LBS)," *IEEE Transactions on Education*, Vol. 31, No. 3, 236–238, 1988.
16. Kim, K. C. and J. Lee, "Comparison of Biot Savart simulation and 3D finite element simulation of the electromagnetic forces acting on end windings of electrical machines," *12th Biennial IEEE Conference on Electromagnetic Field Computation, CEFC 2006*, Vol. 135, No. 6, 4244, 2006.
17. Landini, M., "About the physical reality of 'maxwell's displacement current' in classical electrodynamics," *Progress In Electromagnetics Research*, Vol. 144, 329–343, 2014.

18. Le-Duc, T., O. Chadebec, J.-M. Guichon, and G. Meunier, "New coupling between PEEC method and an integro-differential approach for modeling solid conductors in the presence of magneticconductive thin plates," *IET 8th International Conference on Computation in Electromagnetics (CEM 2011)*, Vol. 19, 30–31, 2011.
19. Le-Van, V., Développement de formulations intégrales de volume en magnétostatique. Ph.D, Université Grenoble Alpes — Laboratoire de Génie Electrique de Grenoble, Grenoble, 2015.
20. Meunier, G., *The Finite Element Method for Electromagnetic Modeling*, John Wiley & Sons, Inc., Hoboken, 2008.
21. Modric, T., S. Vujevic, and D. Lovric, "3D computation of the power lines magnetic field," *Progress In Electromagnetics Research M*, Vol. 41, 1–9, 2015.
22. Nunes, A. S., O. Chadebec, P. Kuo-Peng, P. Dular, and G. Meunier, "A coupling between the facet finite element and reluctance network methods in 3-D," *IEEE Transactions on Magnetics*, Vol. 53, No. 10, 1–10, October 2017.
23. Suh, J.-C., "The evaluation of the biot-savart integral," *Journal of Engineering Mathematics*, Vol. 37, No. 4, 375–395, 2000.
24. Urankar, L., "Vector potential and magnetic field od current-carrying finite arc segment in analytical form, Part III: Exact computation for rectangular cross section," *IEEE Transactions on Magnetics*, Vol. 18, No. 6, 1860–1867, 1982.
25. Urankar, L., "Vector potential and magnetic field of current-carying finite arc segment in analytical form, part II: Thin sheet approximation," *IEEE Transactions on Magnetics*, Vol. 18, No. 3, 911–917, May 1982.
26. Urankar, L., "Vector potential and magnetic field of current-carrying finite arc segment in analytical form, part IV: General three-dimensional current density," *IEEE Trans. Magn.*, Vol. 20, No. 6, 2145–2150, November 1984.
27. Urankar, L., "Vector potential and magnetic field of current-carrying circular finite arc segment in analytical form — Part V. Polygon cross section," *IEEE Transactions on Magnetics*, Vol. 26, No. 3, 1171–1180, May 1990.
28. Urankar, L. and P. Henninger, "Compact extended algorithms for elliptic integrals in electromagnetic field and potential computations. I. Elliptic integrals of the first and second kind with extended integration range," *IEEE Transactions on Magnetics*, Vol. 27, No. 5, 4338–4342, September 1991.
29. Volkmar, C., T. Baruth, J. Simon, U. Ricklefs, and R. Thueringer, "Arbitrarily shaped coils' inductance simulation based on a 3-dimensional solution of the Biot-Savart law," *Proceedings of the International Spring Seminar on Electronics Technology*, No. 1, 210–215, 2013.
30. Weggel, C. F. and D. P. Schwartz, "New analytical formulas for calculating magnetic field," *IEEE Transactions on Magnetics*, Vol. 24, No. 2, 1544–1547, March 1988.
31. Wilton, D., S. Rao, A. Glisson, D. Schaubert, O. Al-Bundak, and C. Butler, "Potential integrals for uniform and linear source distributions on polygonal and polyhedral domains," *IEEE Transactions on Antennas and Propagation*, Vol. 32, No. 3, 276–281, March 1984.
32. Wu, J.-Z., H.-Y. Ma, and M.-D. Zhou, *Vorticity and Vortex Dynamics*, Springer Berlin Heidelberg, 2007.